Enhanced electrocatalytic activity of PtRu/nitrogen and sulphur co-doped crumbled graphene in acid and alkaline media

Liuqing Pang,[1] Yuanyuan Miao,[1] Siddheshwar N. Bhange,[2] Alexandre Barras,[1] Ahmed Addad,[3] Pascal Roussel,[4] Mohammed A. Amin,[5,6*] Sreekumar Kurungot,[2] Sabine Szunerits,[1] and Rabah Boukherroub[1*]

[1]*Univ. Lille, CNRS, Centrale Lille, Univ. Polytechnique Hauts-de-France, UMR 8520, IEMN, F-59000 Lille, France*

[2] *Physical & Materials Chemistry Division, CSIR-National Chemical Laboratory, Pune, Maharashtra, India*

[3]*Univ. Lille, CNRS, UMR 8207 – UMET, F-59000 Lille, France*

[4] *Univ. Lille, CNRS, ENSCL, Centrale Lille, Univ. Artois, UMR8181, UCCS-Unité de Catalyse et Chimie du Solide, Lille, F-59000, France*

[5]*Department of Chemistry, College of Science, Taif University, P.O. Box 11099, Taif 21944, Saudi Arabia*

[6]*Department of Chemistry, Faculty of Science, Ain Shams University, 11566 Abbassia, Cairo, Egypt*

*To whom correspondence should be addressed: Mohammed A. Amin (mohamed@tu.edu.sa); Rabah Boukherroub (rabah.boukherroub@univ-lille.fr); Tel: +333 62 53 17 24

Abstract

The high cost and low mass activity of pure platinum (Pt)-based catalysts predominantly limit their large-scale utilization in electrocatalysis. Therefore, the reduction of Pt amount while preserving the electrocatalytic efficiency represents a viable alternative. In this work, we prepared new $PtRu_2$ nanoparticles supported on sulphur and nitrogen co-doped crumbled graphene with trace amounts of iron ($PtRu_2$/PF) electrocatalysts. The $PtRu_2$/PF catalysts exhibited enhanced electrocatalytic activity and durability for hydrogen evolution reaction (HER) at pH=0. Moreover, the prepared $PtRu_2$/PF electrocatalyst displayed higher HER than commercial 20% Pt/C. The $PtRu_2$/PF catalyst achieved a current density of 10 $mA \cdot cm^{-2}$ at a low overpotential value of only 22 mV for HER, performing better activity than many other Pt-based electrocatalysts. Besides, the $PtRu_2$/PF revealed a good performance for the oxygen evolution reaction (OER) and oxygen reduction reaction (ORR) in alkaline media. The $PtRu_2$/PF catalyst recorded a current density of 10 mA cm^{-2} at an overpotential of only 270 mV for OER in 1.0 M KOH solution and an onset potential of 0.96 V *vs.* RHE (at 1 mA cm^{-2}) for ORR in 0.1 M KOH solution.

Keywords: *$PtRu_2$; sulphur and nitrogen co-doped crumbled graphene; HER; OER; ORR.*

1. Introduction

Platinum supported on carbon (Pt/C) is a widely used electrocatalyst for hydrogen evolution reaction (HER), owing to its low overpotential and enhanced stability in harsh environment [1-3]. Despite these favorable properties, the extremely high price and low natural abundance have severely constrained Pt large-scale industrial application [4-6]. In order to make fuel cells commercially viable, several strategies have been attempted through the reduction of Pt amount or using non-noble metal electrocatalysts without sacrificing their performance. The best performing non-noble metal electrocatalysts reported often contain a transition metal cation such Fe [7-8], Co [9-10] or Ni [11-12]. Unfortunately, their Tafel slopes (thus kinetics) and overpotential values are still higher than those of common Pt-based catalysts for HER. To achieve low Tafel slopes and small overpotentials, high loadings of these non-precious catalysts are required [13], preventing their widespread usage in fuel cells.

Reduction of Pt amount while preserving the electrocatalytic efficiency is another viable alternative. Over the past decade, countless attempts have been devoted to research for the reduction of the amount of Pt, which in turn allows reducing the cost [14]. From the literature survey, introducing one or several different metals to contact with single-phase Pt nanomaterials has brought great hope to alleviate the above challenges, owing to their dramatic enhancement of the electrocatalytic properties and stability, as compared to single element Pt catalyst. For example, Sun and Chang demonstrated that ultrathin two-dimensional CoFePt alloy materials exhibited high catalytic activity towards the HER with an overpotential of 18 mV to achieve a current density of 10 mA cm^{-2} [15]. Liang *et al.* demonstrated that tuning the atomic segregation of Pt-Ni catalysts represents an effective way to optimize their H and OH adsorption abilities, thus enhancing the alkaline HER performance [16]. Liu *et al.* prepared controlled Pt monolayer catalyst on complex 3D structures for superior HER [17-19]. In general, in most of these methods, a similar strategy

was adopted, consisting of Pt loading onto large specific surface area materials and highly dispersible nanomaterials with the aim to reduce the Pt amount [20-24]. However, these approaches need strict technical requirements and are associated with expensive production costs. Additionally, the low stability of these catalysts also restricts their performance for fuel cell applications, because this could eventually lead to a substantial catalytic activity loss, meaning that these catalysts need to be replaced soon upon their utilization. In order to increase the efficiency, the electrocatalyst should exhibit good stability, high activity, and low cost.

In this study, we describe the synthesis of high-performance Platinum-Ruthenium (Pt-Ru) nanoparticles loaded on sulphur- and nitrogen-co-doped crumbled graphene derived from polyethylenedioxythiophene with trace amount of Fe (PF) [25]. These catalysts have several merits as the amount of Pt used was reduced to a minimum, and Ru being relatively cheap (~ 4% of Pt) and displaying a comparable bond strength for hydrogen as Pt. PF was investigated as the support, owing to its corrosion resistance and high surface area (**Fig. 1**). Interestingly, the $PtRu_2$/PF catalyst, with a small amount of Pt, displayed improved performance than the catalyst with higher Pt loading (PtRu/PF) for catalyzing HER under acidic conditions. Additionally, the catalyst also had an excellent performance for oxygen reduction reaction (ORR) and oxygen evolution reaction (OER) in alkaline media compared to many reported noble-metal catalysts.

Figure 1. Fabrication process of Pt and Ru nanoparticles supported on sulphur- and nitrogen-co-doped crumbled graphene (PF) electrocatalysts.

2. Experimental Part

2.1 Materials

Ruthenium (III) chloride ($RuCl_3$), potassium tetrachloroplatinate(II) (K_2PtCl_4), iron chloride hexahydrate ($FeCl_3 \cdot 6H_2O$), dimethylformamide (DMF), methanol (MeOH), cetyltrimethylammonium bromide (CTAB), ammonium persulfate [$(NH_4)_2S_2O_8$], ethylenedioxythiophene (EDOT), platinum on graphitized carbon (20% Pt/C), ruthenium dioxide (RuO_2), hydrochloric acid (HCl), potassium hydroxide (KOH), and sulfuric acid (H_2SO_4, 98%) were purchased from Sigma-Aldrich, France, and used without further purification.

2.2 Preparation of sulphur- and nitrogen-co-doped crumbled graphene with trace amounts of iron (PF)

Sulphur- and nitrogen-co-doped crumbled graphene with trace amounts of iron (PF) was prepared according to a previously reported procedure [25]. Briefly, 2 mL of EDOT monomer were dissolved in 80 mL of 1 M HCl solution using 1 g of CTAB surfactant at room temperature. A solution of 5 g of $(NH_4)_2S_2O_8$ in 20 mL of 1 M HCl was added dropwise to the EDOT solution, followed by the addition of 9.1 g of $FeCl_3 \cdot 6H_2O$ solution in 20 mL of 1 M HCl solution. The resulting mixture was kept under constant stirring for a period of 24 h. The suspension containing the polymer and transition metal salt was dried at 80 ^oC with stirring. This product was termed as PEDOT-Fe. The PEDOT-Fe was subsequently annealed for 1 h at 900 ^oC in an argon atmosphere for the carbonization. The resulting black colored powder was dispersed in 0.5 M H_2SO_4 and stirred at 80 ^oC for 8 h to remove residual Fe. The acid-washed sample was further annealed at 900^oC for 1 h in Ar atmosphere to yield the final product. The product, named as PF, represents the annealed PEDOT-Fe.

2.3 Preparation of Pt_m/Ru_n/PF electrocatalysts

60 mg of PF were dispersed in 36 mL of DMF and 9 mL of methanol by sonication for 30 min. In this reaction, DMF and methanol act as stabilizing and dispersing agents, respectively. Then a mixture of n mg of $RuCl_3$ (n=30, 20, 15, 0) and m mg of K_2PtCl_4 (m=0, 10, 15, 30) were added into the solution under vigorous stirring. The resulting mixture was transferred into a Teflon-lined stainless-steel vessel (50 mL) and heated for 15 h at 160 °C. The products (Pt_mRu_n/PF) were collected by centrifugation, washed with methanol (three times) and dried at 60 °C for overnight.

3. Results and discussion

3.1 Synthesis and characterization of Pt_mRu_n/PF electrocatalysts

The sulphur- and nitrogen-co-doped crumbled graphene with trace amounts of iron (PF) was prepared according to a previously reported procedure [25]. Then a mixture of n mg of $RuCl_3$ (n=30, 20, 15, 0), m mg of K_2PtCl_4 (m=0, 10, 15, 30), 60 mg of prepared PF, 36 mL of DMF, and 9 mL of methanol was heated for 15 h at 160 °C. The products (using the original mass ratio of K_2PtCl_4 and $RuCl_3$ named as Pt_mRu_n/PF) were collected and dried at 60 °C for overnight. The electrocatalytic activity of the obtained catalysts was assessed for HER in acidic medium. The results revealed that $PtRu_2$/PF was the most performing material. Therefore, this electrocatalyst was characterized in details throughout this work.

Scanning electron microscopy (SEM) was applied to analyze the microstructure of PF and $PtRu_2$/PF samples. After deposition of Pt and Ru, no obvious change of the surface morphology of PF could be seen. This is most likely ascribed to the small size of Pt and Ru particles (**Fig. 2a** and **2b**). At the same time, small amounts of Pt and Ru are loaded onto the surface of PF substrate or intercalated into PF layers.

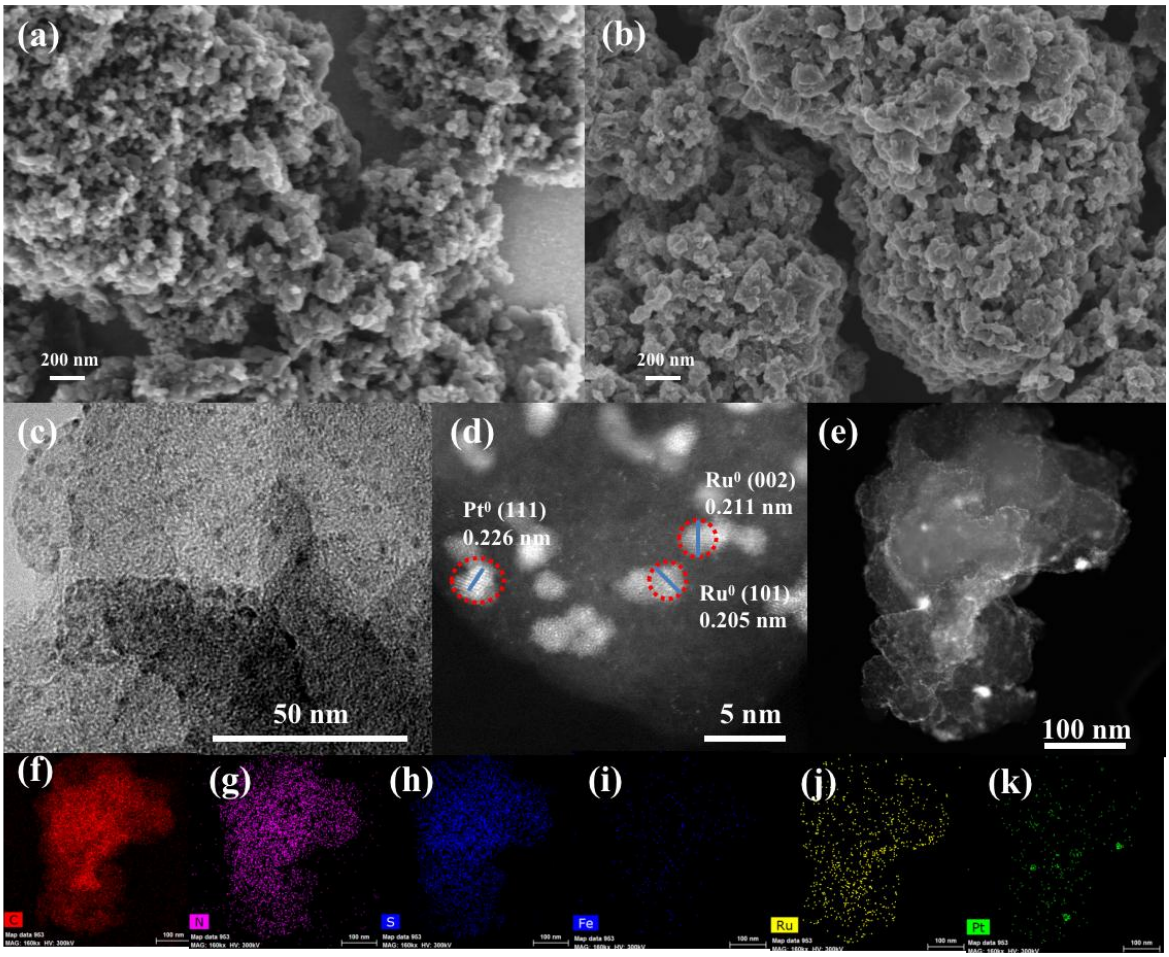

Figure 2. Typical SEM images of (a) PF and (b) $PtRu_2$/PF, (c) TEM and (d) HRTEM images of $PtRu_2$/PF, (e) HAADF-STEM image of $PtRu_2$/PF, (f-k) the corresponding EDX maps of (f) C, (g) N, (h) S, (i) Fe, (j) Ru and (k) Pt obtained from the region in (e).

Additionally, the edges of graphene sheets from the PF were further observed from the transmission electron microscopy (TEM) images. **Figure 2c** depicts the high-resolution TEM image of $PtRu_2$/PF. It shows a uniform structure consisting of thin graphene sheets, and not many large particles are found. Small nanoparticles (2-3 nm) of Ru and Pt can be easily identified with lattice spacings of 0.205, 0.211 and 0.226 nm, which are consistent with the (101) and (002) facets of the Ru^0 crystal (PDF 06-0663) and the (111) facet of the Pt^0 crystal (PDF 87-0646), respectively (**Fig. 2d**). **Figure 2e** shows a transparent graphene sheet

structure, implying that no large particles were formed under these experimental conditions. Furthermore, energy-dispersive X-ray spectroscopy (EDX) mapping was performed to study the distribution of the C, N, S, Fe, Ru and Pt elements in $PtRu_2$/PF sample. All the mapping images (**Fig. 2f-k**) present the same profile as that shown in the rectangular area (**Fig. 2e**), indicating that these elements are homogeneously distributed on the PF surface. In addition, the spots originating from Pt particles are fairly less as compared to Ru particles, and are spread randomly throughout the PF, suggesting that the Pt content is lower than that of Ru, and Ru and Pt are finely dispersed (**Fig. 2j** and **2k**).

Figure 3a depicts the X-ray diffraction (XRD) patterns of PF and $PtRu_2$/PF electrocatalyst. The XRD pattern of PF depicts a broad peak at 25.3° ascribed to the (002) plane of graphitic carbon, and a relatively weak diffraction peak at 44.1° assigned to the (101) plane, in good agreement with earlier report [26]. The XRD pattern of $PtRu_2$/PF reveals the presence of an intense and large peak located at ~25.3° assigned to C (002), and another broad peak between 38° ~ 46° corresponding to an overlap of Ru (100) (38.4°), Ru (002) (42.2°), Ru (101) (44.0°), Pt (111) (40.1°) and Pt (200) (45.38°) in $PtRu_2$/PF (PDF 87-0646 for Pt and PDF 06-0663 for Ru). This is due to the broadening of the main Ru peak, indicating that Ru nanoparticles contain still much more crystallites than Pt.

The Raman spectra of both PF and $PtRu_2$/PF display two bands at ~1340 and 1580 cm^{-1} (**Fig. 3b**) assigned respectively to the disorder-induced D band and the tangential mode G band from PF. It was found that $PtRu_2$/PF had a lower I_D/I_G (0.81) than PF (1.03), signifying that $PtRu_2$/PF has structural low defects.

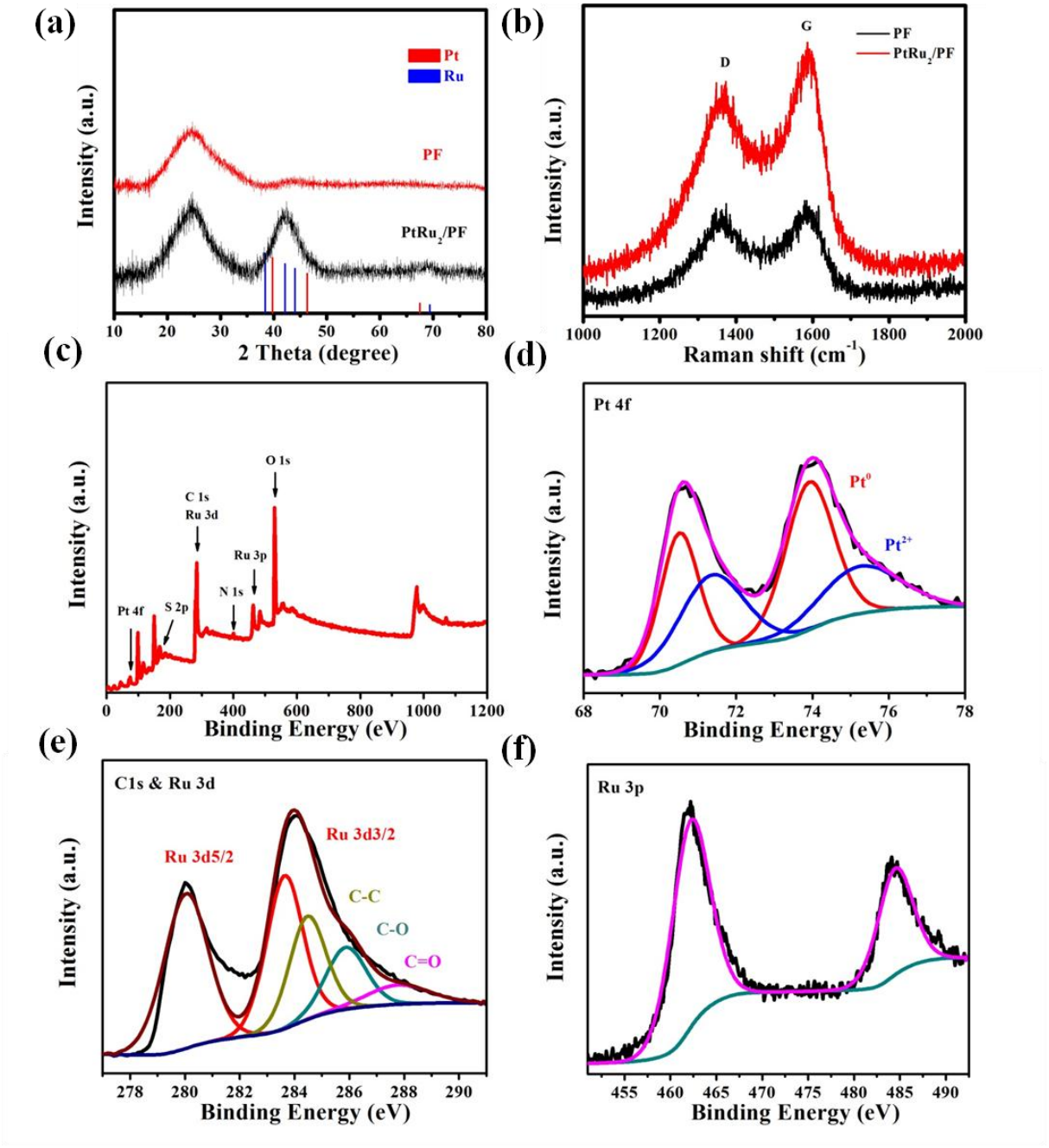

Figure 3. (a) XRD patterns, and (b) Raman spectra of PF and $PtRu_2$/PF. (c) XPS full scan and core level spectra of (d) Pt 4f, (e) C 1s and Ru 3d, and (f) Ru 3p of $PtRu_2$/PF.

X-ray photoelectron spectroscopy (XPS) analysis revealed the expected C, N, S, Ru and Pt in $PtRu_2$/PF composite (**Fig. 3c**). In **Figure 3d**, the high-resolution XPS spectrum of the Pt_{4f} showed doublet peaks at 71.8 and 75.2 eV, which can be deconvoluted into two bands. The deconvoluted doublet bands at 71.2 and 74.6 eV, and 72.1 and 76.0 eV can be ascribed to Pt^0

and Pt^{2+}, respectively [27]. In the C_{1s} and Ru_{3d} XPS core level spectrum (**Fig. 3e**), the bands at 279.9 and 283.6 eV can be attributed to $Ru_{3d5/2}$ and $Ru_{3d3/2}$ of Ru(0), respectively [28]. The C_{1s} peak can be curve-fitted with three peaks centered at 284.5, 286.1 and 287.6 eV, corresponding to the C=C/C-C, C-O and C=O bonds, respectively. The core level XPS spectrum of the Ru_{3p} can be curve-fitted with two bands at 461.4 and 483.8 eV, respectively (**Fig. 3f**), confirming the metallic character of Ru(0) in $PtRu_2$/PF nanocomposite [29].

To further determine the Pt and Ru content in the $PtRu_2$/PF sample, we performed inductive coupled plasma emission spectrometry (ICP-AES) measurements. The results confirmed the prevalence of Ru (72.4 mg/g) over Pt (28.3 mg/g) content in the $PtRu_2$/PF sample. The Ru/Pt mass ratio is ~2.6, which is slightly higher than the theoretical value of 2. In addition, the average precious metal mass per square centimeter of the working electrode is 4.0 μg/cm^2 for Pt and 10.4 μg/cm^2 for Ru.

3.2 Electrocatalytic activity for the hydrogen evolution reaction (HER)

The electrocatalytic HER activity of the synthesized Pt-based catalysts (PF, Ru/PF, $PtRu_2$/PF,PtRu/PF,Pt/PF and 20% Pt/C) was assessed in H_2SO_4 (0.5 M) aqueous solution using linear sweep voltammetry (LSV) measurements (**Fig. 4a**). For comparison to the literature, the measured potentials were converted to that relative to the reversible hydrogen electrode (RHE) according to equation 1:

$$E_{RHE} = E_{Ag/AgCl} + E^{\circ}_{Ag/AgCl} + 0.059 \times \text{pH} \qquad (1)$$

pH = 0 and $E^{\circ}_{Ag/AgCl}$ = 0.2046 V (25°C).

From the first sight, it seems that the investigated catalysts are very effective for hydrogen evolution. This is clear from their low HER onset potential (E_{HER}, the potential at which the current starts to rise and a reaction starts to take place) values (**Table S1**) and steep cathode polarization curves beyond E_{HER}. The results identified that the $PtRu_2$/PF, PtRu/PF, Pt/PF and

20% Pt/C catalysts exhibited low E_{HER} values, all around -0.01 V_{RHE}, and high cathode currents beyond E_{HER}. These findings reveal the ability of these catalysts to generate significant amount of hydrogen gas at low overpotentials, thus reflecting their high catalytic HER activity. On the contrary, Ru/PF and PF exhibited inferior catalytic activity for the HER, as they recorded significantly higher E_{HER}, namely -0.06 and -0.16 V_{RHE}, respectively. Moreover, by comparing the current density changes at any applied overpotential, the $PtRu_2$/PF exhibited clear advantages over the potential range from 0.05 to -0.30 V_{RHE}. For instance, the $PtRu_2$/PF catalyst achieved a current density of -75 $mA \cdot cm^{-2}$ at E = -0.1 V_{RHE}, higher than that derived from the PtRu/PF catalyst (-58 $mA \cdot cm^{-2}$) at the same overpotential. The current densities from other catalysts, namely PF, Ru/PF, Pt/PF and 20% Pt/C are markedly much smaller: -0.5, -12, -44 and -57 $mA \cdot cm^{-2}$, respectively. At any given current density, the overpotential was shifted toward less negative values (active direction), following the sequence: Ru/PF > Pt/PF > 20% Pt/C ≥ PtRu/PF ≥ $PtRu_2$/PF. The overpotential necessary to achieve a current density of -10 $mA \cdot cm^{-2}$ (η_{10}), an important electrochemical parameter to evaluate and compare the HER performance of electrocatalysts [30], was determined for all investigated materials. For instance, $PtRu_2$/PF recorded η_{10} value of 22 mV, which is comparable to that determined for PtRu/PF (22 mV) and 20% Pt/C (30 mV). This anodic shift in E_{HER} refers generally to accelerated HER kinetics at low overpotentials [31]. Therefore, the results confirm the superior HER activity of the $PtRu_2$/PF catalyst.

The active drift in E_{HER} is also translated into increased exchange current density (J_o), i.e., enhanced HER kinetics [32]. This is clear from **Table S1**; the promising catalytic activity of $PtRu_2$/PF catalyst was also confirmed, as it recorded enhanced J_o value among the tested catalysts.

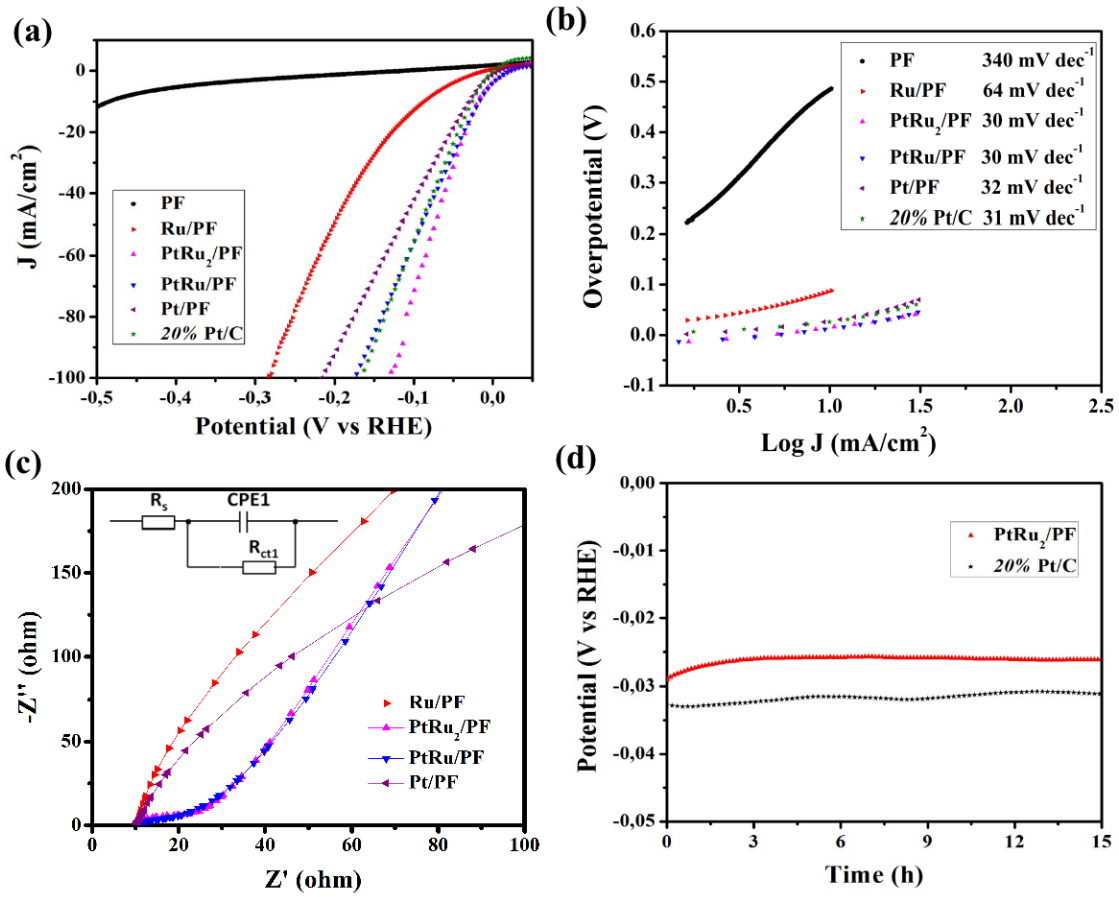

Figure 4. Electrochemical characterization. (a) HER polarization curves, scan rate = 20 mV s^{-1}, (b) Tafel plots, (c) EIS Nyquist plots of the different electrocatalysts recorded over the frequency range of 100 kHz to 0.06 Hz in 0.5 M H_2SO_4 aqueous solution at 0.1 V; the inset is the equivalent circuit, and (d) HER stability test of $PtRu_2$/PF and 20% Pt/C at J=-10 mA/cm^2 in H_2SO_4 (0.5 M) aqueous solution.

The Tafel slope (β_c), calculated *via* fitting the linear segments of the Tafel plots, gives a good measure of the intrinsic properties of electrocatalytic materials [33]. As shown in **Figure 4b**, Pt/PF and Ru/PF catalysts recorded β_c values of 32 and 64 mV dec^{-1}, respectively, which are very close to those reported for Pt/C (30 mV dec^{-1}) and Ru/MeOH/THF (46 mV dec^{-1}) [34]. In contrast, a high β_c value of 340 mV dec^{-1} was measured for PF, revealing its inferior catalytic activity. For $PtRu_2$/PF and PtRu/PF catalysts, the measured β_c values are around 30

mV dec^{-1}, signifying much improved HER activity, as lower β_c values reveal increased number of catalytically active sites [35].

The overall HER reaction mechanism in acidic media could occur through a discharge step (Volmer-reaction, 120 mVdec^{-1}), followed by ion or atom reaction (Heyrovsky reaction, 40 mV dec^{-1}) or a combination reaction (Tafel reaction, 30 mV dec^{-1}) [36]. It was proposed that, at a very high surface coverage of adsorbed hydrogen (H_{ads}), the HER on the Pt surface is controlled by Volmer-Tafel mechanism, with the recombination step being the slowest (rate-determining) step, as evidenced from the recorded Tafel slope (30 mV dec^{-1}) [37]. Based on this, the small Tafel slope (~30 mV dec^{-1}) recorded for $PtRu_2$/PF and PtRu/PF catalysts suggests a HER mechanism similar to that occurred on Pt.

The Electrochemical Impedance Spectroscopy (EIS) studies corroborate previously presented results (**Fig. S1)**. The Bode plots (**Fig. S1a, b**) reveal the presence of two relaxation times. The total impedance |Z| remains the smallest for analyzed Ru-enriched materials, with negligible differences between PtRu/PF and $PtRu_2$/PF samples. On the other hand, its value is nearly an order of magnitude higher for Pt/PF sample at a wide frequency range. Both PtRu/PF and $PtRu_2$/PF electrodes demonstrate a decrease of the phase angle and a shift into higher frequency range as compared to Pt/PF electrode, testifying the enhanced electron transfer kinetics. In addition, the charge transfer kinetics appears to be the most sluggish through the Ru/Pt electrodes. Similar characteristics are often seen when studying the catalysts at increased overpotentials [38,39].

The Nyquist plots in **Figure 4c** confirm the above conclusions. The high frequency semicircle present on the analyzed spectra reflects the charge transfer process of hydrogen evolution reaction [39,40]. The inclined line, at low frequencies, indicates the electron diffusion behavior on the electrode interface, representative of a diffusion-controlled process [41-43]. The value of the charge transfer resistance R_{ct} was determined to be ~15 and 20

Ω/cm^2 for PtRu/PF and $PtRu_2$/PF electrodes, respectively [44]. For comparison, the R_{ct} of Ru-free Pt/PF electrode was roughly 800 Ω/cm^2. The significant decrease of the charge transfer resistance as a result of Ru incorporation testifies the faster reaction rates and the enhanced electrocatalytic properties of the material. The enhanced activity towards HER resulting from Ru incorporation was also reported in previous studies [45]. The reduced R_{ct} of $PtRu_2$/PF and PtRu/PF may be explained by the interaction and synergy of the two metals. The better electron transfer ability of $PtRu_2$/PF and PtRu/PF are also expected to contribute to their enhanced HER catalytic activity [46].

The stability is an important feature for the HER catalysts. Therefore, the stability of $PtRu_2$/PF and *20%* Pt/C catalysts was assessed at a controlled current density (J = -10 $mA \cdot cm^{-2}$) for 15 h in H_2SO_4 (0.5 M) aqueous solution (**Fig. 4d**); the overpotential of the $PtRu_2$/PF catalyst was more stable than that of 20% Pt/C under our experimental conditions, suggesting its good stability [17, 21].

The electrochemical active surface area (ECSA) of these catalysts was estimated from cyclic voltammetry (CV) measurements, conducted in H_2SO_4 (0.5 M) aqueous solution at various potential scan rates (ca. 30 - 80 mV s^{-1}) from 0.15 to 0.45 V *vs.* RHE (**Fig. S2 a-e**). The CVs display a pseudo-rectangular shape without any apparent Faradic processes. The current density values, determined at 0.30 V (*vs.* RHE) from the CV, were then plotted as a function of the scan rate. From the results in **Fig. S2f**, the C_{dl} of $PtRu_2$/PF and PtRu/PF were determined to be as 38 and 37 mF cm^{-2}, larger than the other catalysts: Pt/PF (24 mF cm^{-2}), Ru/PF (16 mF cm^{-2}) and PF (8 mF cm^{-2}). A higher C_{dl} value correlates with more exposed active sites, which is favorable for electrochemical processes. From the above results, we can conclude that $PtRu_2$/PF exhibits more active sites than PtRu/PF [47]. The values of C_{dl} were inserted in Eq. (2) to calculate the ECSA values [48]:

$$ECSA = C_{dl} / C_s \quad (2)$$

C_s is the electrode's specific capacitance with a flat standard surface area of 1.0 cm^{-2}, typically between 20 and 60 μF cm^{-2} [48]. Using 40 μF cm^{-2} as the averaged capacitance value for the flat electrode, ECSA values of 200, 400, 600, 925 and 950 sites per cm^2 were calculated for PF, Ru/PF, Pt/PF, PtRu/PF and $PtRu_2$/PF, respectively.

Active sites density calculations

Figure 5 depicts typical cyclic voltammetry measurements for PF, Ru/PF, Pt/PF, PtRu/PF, and $PtRu_2$/PF catalysts conducted in H_2SO_4 (0.5 M) aqueous solution at a scan rate of 100 mV s^{-1} at room temperature. The number of active sites (n) in PtRu/PF and $PtRu_2$/PF catalysts was determined from such measurements, using Eq. (3) [49]:

$$n = (Q/2F) \times N_A \qquad (3)$$

$N_A = 6.022\times10^{23}$ mol^{-1} is the Avogadro's number, the number 2 is the stoichiometric number of electrons consumed during the HER reaction, and F is the Faraday constant (96485 C/mol). Q is the net voltammetry charge of the catalyst, estimated *via* subtracting charges resulting from the bare PF electrode (the black cyclic voltammogram in **Fig. 5**). Q values of 4.05×10^{-2} and 5.8×10^{-2} C were recorded for PtRu/PF and $PtRu_2$/PF catalysts, respectively. Inserting such Q values into Eq. (3) gives n values of 1.26×10^{17} and 1.81×10^{17} Ru sites per cm^2, respectively.

The averaged area ($A_{average}$) to find one Ru center (cm^2 per site) can be calculated *via* dividing the PtRu/PF and $PtRu_2$/PF catalysts' ECSA values by the value of n (Ru sites per cm^2). This gives $A_{average}$ values of 7.34×10^{-15} and 5.25×10^{-15} cm^2 per Ru for PtRu/PF and $PtRu_2$/PF, respectively. The reciprocal of $A_{average}$ per site yields the active sites density (sites / cm^2) [50]. Based on this, active sites density values of 1.36×10^{13} and 1.9×10^{14} sites/cm^2 were estimated for PtRu/PF and $PtRu_2$/PF, respectively. Following the same sequence of calculations for the two catalysts with the individual active materials, namely Ru/PF and

Pt/PF (where Q values of 0.88×10^{-3} and 1.36×10^{-3} C were recorded for Ru/PF and Pt/PF, respectively) gave active sites density values of 6.89×10^{11} and 7.04×10^{12} sites/cm^2, respectively. These results provide an additional evidence for the effective catalytic impact of Ru in the PtRu/PF catalyst, which further enhanced with increasing Ru content, as in the $PtRu_2$/PF catalyst which exhibited the best catalytic performance amongst.

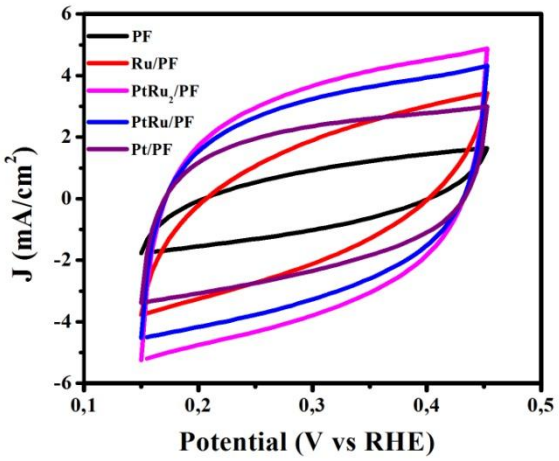

Figure 5. Cyclic voltammograms of the synthesized catalysts acquired in the 0.15 ~ 0.45 V potential range *vs.* RHE in H_2SO_4 (0.5 M) aqueous solution; scan rate=100 mV s^{-1} at room temperature.

3.3 Oxygen evolution reaction (OER)

Oxygen evolution reaction (OER) and oxygen reduction reaction (ORR) are also the key processes in electrochemical energy storage and energy conversion applications. In this line, the electrocatalytic performance of $PtRu_2$/PF catalyst was investigated for OER in KOH (1.0 M) aqueous solution. **Figure 6a** depicts the LSV curves of Ru/PF, $PtRu_2$/PF, PtRu/PF, Pt/PF and commercial 20% Pt/C catalysts at 5 mV s^{-1}. In comparison with Ru/PF (305 mV), Pt/PF (390 mV) and RuO_2 (280 mV) catalysts at 10 mA cm^{-2}, PtPtRu/PF and PtPtRu_2/PF catalysts achieved enhanced OER activity with overpotential values close to 270 mV at the same

current density. These results reveal the promising OER catalytic performance of PtPtRu/PF and $PtPtRu_2$/PF catalysts thus, highlighting the effective catalytic influence of Ru on the OER too. According to the literature, the OER mechanism in alkaline electrolytes over a catalytically active site (*S**) can be represented by Eqs. 4-7 [51].

$$OH^- + S^* \rightarrow S^*OH + e^- \quad (4)$$

$$S^*OH + OH^- \rightarrow S^*O^- + H_2O \quad (5)$$

$$S^*O^- \rightarrow S^*O + e^- \quad (6)$$

$$S^*O + S^*O \rightarrow S^* + S^* + O_2 \quad (7)$$

OH^- adsorption on *S** is found to play a fundamental role in enhancing the OER kinetics. Such catalytically active site (*S**) is proven to accelerate the adsorption and desorption of the OH^- anions [51]. Electrochemical characterizations shown above revealed the efficacious catalytic role of Ru in the PtRu/PF catalyst, which further enhanced with increase in Ru content, in accelerating the OER kinetics. Based on this, the Ru atoms in the PtRu/PF catalyst are expected to act as active catalytic sites for the OER *via* hastening the adsorption and desorption of the OH^- anions. This, in turn, boosts the kinetics of the OER, resulting in reduced Tafel slopes values [51]. PtRu/PF and $PtRu_2$/PF catalysts recorded reduced Tafel slope values of 79 mV dec^{-1}. This value is very close to that measured here for the OER state-of-the-art electrocatalyst, namely RuO_2 (78 mV dec^{-1}), suggesting fast OER kinetics on PtRu/PF and $PtRu_2$/PF catalysts.

The PtRu/PF and $PtRu_2$/PF catalysts' OER mass activities were also calculated to further confirm their outstanding catalytic performance compared with the other tested electrocatalysts. Mass activity of the OER is given by the ratio j/c, where j is the current density produced at a specific potential and c is the catalyst loading density on the GC

electrode, 0.143 × 10^{-3} g cm^{-2}. Pt/PF, Ru/PF, PtRu/PF, and $PtRu_2$/PF catalysts generated an anodic current density of 0.057, 0.094, 0.16, 0.18 A cm^{-2} at 1.8 V *vs.* RHE, respectively. Based on this, OER mass activities of 398.6, 657.3, 1119, and 1259 A g^{-1} were calculated for Pt/PF, Ru/PF, PtRu/PF, and $PtRu_2$/PF catalysts, respectively. The PtRu/PF, and $PtRu_2$/PF catalysts's mass activities (1119, and 1259 A g^{-1} @ 1.8 V *vs.* RHE) exceeded that of the state-of-the-art RuO_2 catalyst (807 A g^{-1}, with 0.115 A cm^{-2} generated @ 1.8 V *vs.* RHE), thus confirming the outstanding catalytic activity of the PtRu/PF, and $PtRu_2$/PF catalysts for the OER.

The LSV measurements were also conducted in O_2-saturated KOH (0.1 M) electrolyte without rotation at a sweeping rate of 20 mV s^{-1} (**Fig. 6c**). The $PtRu_2$/PF displayed the highest current intensity and onset potential among all the catalysts. The onset potential (E_{onset}) is regarded as the potential recorded at a current density of -1 mA cm^{-2} in the LSV. The E_{onset} of $PtRu_2$/PF (0.96 V) is positive than those of PtRu/PF (0.93 V), Pt/PF catalyst (0.92 V), *20%* Pt/C (0.94 V), and Ru/PF (0.91 V) *vs.* RHE.

Furthermore, we performed the rotating disk electrode (RDE) polarization curves of the $PtRu_2$/PF catalyst in KOH (0.1 M) to gain more insights about the ORR kinetics and catalytic mechanism in alkaline medium from 400-2000 rpm (**Fig. 6d**). The limit current density increases from 3.4 to 7.7 mA·cm^{-2} as the rotating speed was varied from 400 to 2000 rpm; it is well established that the high speeds shorten the O_2 diffusion distance in the O_2-saturated electrolyte. The corresponding Koutecky-Levich (K-L) plots (**Fig. 6e**) within the 0.3 to 0.7 V potential range *vs.* RHE displayed good linearity, which confirms first-order reaction kinetics, and the number of electrons transferred (n) during the reaction are the same at different potentials. Additionally, the determined value of n is 3.9 ~ 4.1 over the investigated potential

window, suggest that the $PtRu_2$/PF catalyst follows the 4 electrons-transfer pathway, which corresponds to a complete reduction of oxygen into water and only little peroxide is formed.

Figure 6f summarizes the ORR [52-59] kinetic data of recent electrodes in 0.1M KOH alkaline solution. It is obvious that $PtRu_2$/PF electrode represents one of the most active electrocatalysts even though most of these noble metal electrocatalysts consist of nanomaterials with high loading amounts and display large surface areas.

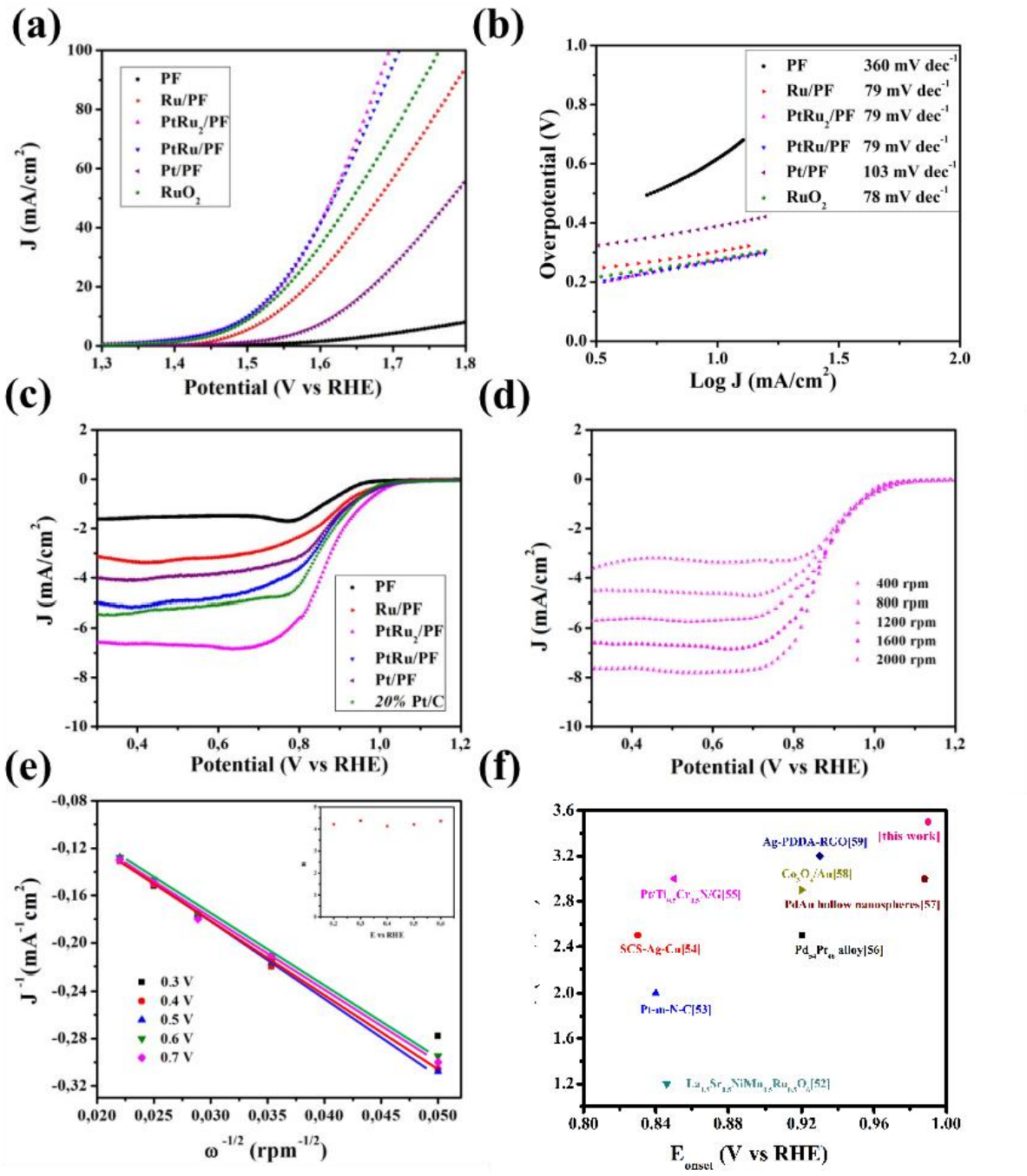

Figure 6. (a) OER polarization curves of Ru/PF, $PtRu_2$/PF, PtRu/PF, Pt/PF, and commercial 20% Pt/C catalysts; The PF-supported catalysts were first cycled (10 cycles) in 0-1 V *vs.* Ag/AgCl potential range at a scan rate of 20 mV s^{-1}. (b) The corresponding Tafel plots calculated from LSV curves in (A). (c) ORR polarization curves of different catalysts with RDE speed =1600 rpm in O_2-saturated KOH (0.1 M) solution, scan rate =20 mV s^{-1}. (d) RDE polarization curves for ORR on $PtRu_2$/PF in O_2-saturated KOH (0.1 M), n=20 mV s^{-1}. (e) K-L plots for ORR in KOH (0.1 M); the inset shows the potential dependence of n. (f) Comparison of the onset potential and current density values of recent reports in KOH (0.1 M) aqueous solution.

4. Conclusion

We have successfully assessed the ultimate limit of Pt in PtRu/PF catalysts*via* a facile hydrothermal approach. The high dispersibility and bimetallic synergy make the $PtRu_2$/PF catalyst have an outstanding HER electrocatalytic activity in acid conditions, considerably better than those reported using a regular Pt-based and commercial *20%* Pt/C catalysts. Furthermore, the $PtRu_2$/PF displayed excellent ORR performance with an onset potential of 0.96 V *vs.* RHE, and a limit current density of 6.5 mA·cm^{-2}, which is better than that of commercial 20% Pt/C (5.3 mA·cm^{-2}). Additionally, the $PtRu_2$/PF also has a superior OER activity. Given that Pt is the most commonly investigated catalyst for many catalytic applications, the results obtained in the present study provide an interesting alternative route to prepare Pt-based catalysts with minimal Pt loading and enhanced electrocatalytic activity. This holds promise for the development of highly efficient and cost-effective electrocatalysts for various electrocatalytic applications.

Acknowledgement

The authors acknowledge financial support from the Centre National de la Recherche Scientifique (CNRS), the University of Lille, and the Hauts-de-France region. L. P and Y. M thank the Chinese government for the China Scholarship Council (CSC) fellowship. The authors are also thankful to the Taif University Researchers Supporting Project number (TURSP-2020/03), Taif University, Taif, Saudi Arabia.

ASSOCIATED CONTENT

Supporting Information

Characterization, Bode plot, Cyclic voltammograms and Table S1.

References

1. S. Bai, C. Wang, M. Deng, M. Gong, Y. Bai, J. Jiang, Y. Xiong, Surface polarization matters: enhancing the hydrogen-evolution reaction by shrinking Pt shells in Pt-Pd-graphene stack structures. Angew. Chem. Int. Ed. 53 (2014) 12120-12124.
2. L. Zhang, L. Wang, C.M.B. Holt, B. Zahiri, Z. Li, K. Malek, T. Navessin, M.H. Eikerling, D. Mitlin, Highly corrosion resistant platinum-niobium oxide-carbon nanotube electrodes for the oxygen reduction in PEM fuel cells. Energy Environ. Sci. 5 (2012) 6156-6172.
3. C. Yang, M. Zhou, Q. Xu, Confining Pt nanoparticles in porous carbon structures for achieving durable electrochemical performance. Nanoscale 6 (2014) 11863-11870.
4. H. Lin, H. Li, Y. Li, J. Liu, X. Wang, L. Wang, Hierarchical CoS/MoS_2 and Co_3S_4/MoS_2/Ni_2P nanotubes for efficient electrocatalytic hydrogen evolution in alkaline media. J. Mater. Chem. A 5 (2017) 25410-25419.

5. X. Ren, L. Pang, Y. Zhang, X. Ren, H. Fan, S. Liu, One-step hydrothermal synthesis of monolayer MoS_2 quantum dots for highly efficient electrocatalytic hydrogen evolution. J. Mater. Chem. A 3 (2015) 10693-10697.
6. L. Pang, A. Barras, Y. Zhang, M. A. Amin, A. Addad, S. Szunerits, R. Boukherroub, CoO Promoted the Catalytic Activity of Nitrogen-doped MoS_2 Supported on Carbon Fiber Mats for Overall Water Splitting. ACS Appl. Mater. Interfaces 11 (2019) 31889-31898.
7. Y. Liu, S. Jiang, S. Li, L. Zhou, Z. Li, J. Li, M. Shao, Interface engineering of (Ni, Fe)S_2@MoS_2 heterostructures for synergetic electrochemical water splitting. Appl. Catal. B 247 (2019) 107-114.
8. E. Isarain-Chavez, M. D. Baro, C. Alcantara, S. Pane, J. Sort, E. Pellicer, Micelle-assisted electrodeposition of mesoporous Fe-Pt smooth thin films and their electrocatalytic activity towards the hydrogen evolution reaction. ChemSusChem 11 (2018) 367-375.
9. Z. Dai, H. Geng, J. Wang, Y. Luo, B. Li, Y. Zong, J. Yang, Y. Guo, Y. Zheng, X. Wang, Q. Yan, Hexagonal-phase cobalt monophosphosulfide for highly efficient overall water splitting. ACS Nano 11 (2017) 11031-11040.
10. Z. Liu, J. Qi, M. Liu, S. Zhang, Q. Fan, H. Liu, K. Liu, H. Zheng, Y. Yin, C. Gao, Aqueous synthesis of ultrathin platinum/non-noble metal alloy nanowires for enhanced hydrogen evolution activity. Angew. Chem. Int. Ed. 57 (2018) 11678-11682.
11. Z. Zhang, G. Liu, X. Cui, B. Chen, Y. Zhu, Y. Gong, F. Saleem, S. Xi, Y. Du, A. Borgna, Z. Lai, Q. Zhang, B. Li, Y. Zong, Y. Han, L. Gu, H. Zhang, Crystal phase and architecture engineering of lotus-thalamus-shaped Pt-Ni anisotropic superstructures

for highly efficient electrochemical hydrogen evolution. Adv. Mater. 30 (2018) 1801741.

12. P. Kuang, T. Tong, K. Fan, J. Yu, In situ fabrication of Ni-Mo bimetal sulfide hybrid as an efficient electrocatalyst for hydrogen evolution over a wide pH range. ACS Catal. 7 (2017) 6179-6187.
13. E. Kemppainen, A. Bodin, B. Sebok, T. Pedersen, B. Seger, B. Mei, D. Bae, P. C. K. Vesborg, J. Halme, O. Hansen, P. D. Lund, I. Chorkendorff, Scalability and feasibility of photoelectrochemical H_2 evolution: the ultimate limit of Pt nanoparticle as an HER catalyst. Energy Environ. Sci. 8 (2015) 2991-2999.
14. N. K. Chaudhari, Y. Hong, B. Kim, S.-I. Choi, K. Lee, Pt-Cu based nanocrystals as promising catalysts for various electrocatalytic reactions. J. Mater. Chem. A 7 (2019) 17183-17203.
15. Q. Zhang, Y. Kuang, Y. Li, M. Jiang, Z. Cai, Y. Pang, Z. Chang, X. Sun, Synthesis and performance optimization of ultrathin two-dimensional CoFePt alloy materials via in situ topotactic conversion for the hydrogen evolution reaction. J. Mater. Chem. A 7 (2019) 9517-9522.
16. C. Zhang, B. Chen, D. Mei, X. Liang, The OH^--driven synthesis of Pt-Ni nanocatalysts with atomic segregation for alkaline hydrogen evolution reaction. J. Mater. Chem. A 7 (2019) 5475-5481.
17. L. Pang, M. Li, Q. Ma, Y. Zhang, X. Ren, D. Zhang, S. F. Liu, Controlled Pt monolayer fabrication on complex carbon fiber structures for superior catalytic applications. Electrochim. Acta 222 (2016) 1522-1527.
18. L. Pang, Y. Zhang, S. Liu, Monolayer-by-monolayer growth of platinum films on complex carbon fiber paper structure. Appl. Surf. Sci. 407 (2017) 386-390.

19. M. Li, Q. Ma, X. Liu, X. Zhu, S. Liu, Pt monolayer coating on complex network substrate with high catalytic activity for the hydrogen evolution reaction. Sci. Adv. 1 (2015) e1400268.
20. J. Q. Chi, J. Y. Xie, W. W. Zhang, B. Dong, J. F. Qin, X. Y. Zhang, J. H. Lin, Y. M. Chai, C. G. Liu, N-Doped sandwich-structured Mo_2C@C@Pt interface with ultralow Pt loading for pH-universal hydrogen evolution reaction. ACS Appl. Mater. Interfaces 11 (2019) 4047-4056.
21. F. Liao, W. Shen, Y. Sun, Y. Li, H. Shi, M. Shao, Nanosponge Pt modified graphene nanocomposites using silicon monoxides as a reducing agent: High efficient electrocatalysts for hydrogen evolution. ACS Sustain. Chem. Eng. 6 (2018) 15238-15244.
22. X. Shang, Z. Z. Liu, S. S. Lu, B. Dong, J. Q. Chi, J. F. Qin, X. Liu, Y. M. Chai, C. G. Liu, Pt-C interfaces based on electronegativity-functionalized hollow carbon spheres for highly efficient hydrogen evolution. ACS Appl. Mater. Interfaces 10 (2018) 43561-43569.
23. J. Theerthagiri, E. S. F. Cardoso, G. V. Fortunato, G. A. Casagrande, B. Senthilkumar, J. Madhavan, G. Maia, Highly electroactive Ni pyrophosphate/Pt catalyst toward hydrogen evolution reaction. ACS Appl. Mater. Interfaces 11 (2019) 4969-4982.
24. L. Zhang, K. Doyle-Davis, X. Sun, Pt-Based electrocatalysts with high atom utilization efficiency: from nanostructures to single atoms. Energy Environ. Sci. 12 (2019) 492-517.
25. S. N. Bhange, S. M. Unni, S. Kurungot, Nitrogen and sulphur co-doped crumbled graphene for the oxygen reduction reaction with improved activity and stability in acidic medium. J. Mater. Chem. A 4 (2016) 6014-6020.

26. X. Liu, W. Zhou, L. Yang, L. Li, Z. Zhang, Y. Ke, S. Chen, Nitrogen and sulfur co-doped porous carbon derived from human hair as highly efficient metal-free electrocatalysts for hydrogen evolution reactions. J. Mater. Chem. A 3 (2015) 8840-8846.
27. J. H. Kim, J. Y. Cheon, T. J. Shin, J. Y. Park, S. H. Joo, Effect of surface oxygen functionalization of carbon support on the activity and durability of Pt/C catalysts for the oxygen reduction reaction. Carbon 101 (2016) 449-457.
28. E. Demir, S. Akbayrak, A. M. Önal, S. Özkar, Nanoceria-supported ruthenium (0) nanoparticles: Highly active and stable catalysts for hydrogen evolution from water. ACS Appl. Mater. Interfaces 10 (2018) 6299-6308.
29. J. Shi, M. Zhao, Y. Wang, J. Fu, X. Lu, Z. Hou, Upgrading of aromatic compounds in bio-oil over ultrathin graphene encapsulated Ru nanoparticles. J. Mater. Chem. A 4 (2016) 5842-5848.
30. J. Benson, M. Li, S. Wang, P. Wang, P. Papakonstantinou, Electrocatalytic hydrogen evolution reaction on edges of a few layer molybdenum disulfide nanodots. ACS Appl. Mater. Interfaces 7 (2015) 14113-22.
31. P. Zhu, Y. Chen, Y. Zhou, Z. Yang, D. Wu, X. Xiong, F. Ouyang, A metallic MoS_2 nanosheet array on graphene-protected Ni foam as a highly efficient electrocatalytic hydrogen evolution cathode. J. Mater. Chem. A 6 (2018) 16458-16464.
32. F. Safizadeh, E. Ghali, G. Houlachi, Electrocatalysis developments for hydrogen evolution reaction in alkaline solutions-A Review. Int. J. Hydrogen Energy 40 (2015) 256-274.
33. Y.-H. Fang, Z.-P. Liu, Tafel kinetics of electrocatalytic reactions: from experiment to first-principles. ACS Catal. 4 (2014) 4364-4376.

34. S. Drouet, J. Creus, V. Colliere, C. Amiens, J. Garcia-Anton, X. Sala, K. Philippot, A porous Ru nanomaterial as an efficient electrocatalyst for the hydrogen evolution reaction under acidic and neutral conditions. Chem. Commun. 53 (2017) 11713-11716.
35. A. P. Murthy, J. Theerthagiri, J. Madhavan, Insights on Tafel constant in the analysis of hydrogen evolution reaction. J. Phys. Chem. C 122 (2018) 23943-23949.
36. C. Lin, C. Batchelor-McAuley, E. Laborda, R. G. Compton, Tafel-Volmer electrode reactions: the influence of electron-transfer kinetics. J. Phys. Chem. C 119 (2015) 22415-22424.
37. W. Ren, H. Zhang, C. Cheng, Ultrafine Pt nanoparticles decorated MoS_2 nanosheets with significantly improved hydrogen evolution activity. Electrochim. Acta 241 (2017) 316-322.
38. L. Liao, S. Wang, J. Xiao, X. Bian, Y. Zhang, M. D. Scanlon, et al. A nanoporous molybdenum carbide nanowire as an electrocatalyst for hydrogen evolution reaction. Energy Environ. Sci. 7 (2014) 387-392.
39. R. K. Shervedani, A. R. Madram, Kinetics of hydrogen evolution reaction on nanocrystalline electrodeposited $Ni_{62}Fe_{35}C_3$ cathode in alkaline solution by electrochemical impedance spectroscopy. Electrochim. Acta 53 (2007) 426-433.
40. A. KalasapurayilKunhiraman, M. Ramasamy, S. Ramanathan, Efficient hydrogen evolution catalysis triggered by electrochemically anchored platinum nano-islands on functionalized-MWCNT. Int. J. Hydrogen Energy 42 (2017) 9881-9891.
41. M. Sun, H. Liu, J. Qu, J. Li, Earth-rich transition metal phosphide for energy conversion and storage. Adv. Energy Mater. 6 (2016) 1600087.

42. M. Farsak, E. Telli, F. Tezcan, F. S. Akgül, A. O. Yüce, G. Kardaş, The electrocatalytic properties of lithium copper composite in the oxygen reduction reaction. Electrochim. Acta 148 (2014) 276-282.
43. E. Telli, M. Farsak, G. Kardaş, Investigation of noble metal loading CoWZn electrode for HER. Int. J. Hydrogen Energy 42 (2017) 23260-23267.
44. M. E. Orazem, N. Pébère, B. Tribollet, Enhanced graphical representation of electrochemical impedance data. J. Electrochem. Soc. 153 (2006) B129-B136.
45. G. Fan, Q. Liu, D. Tang, X. Li, J. Bi, D. Gao, Nanodiamond supported Ru nanoparticles as an effective catalyst for hydrogen evolution from hydrolysis of ammonia borane. Int. J. Hydrogen Energy 41 (2016) 1542-1549.
46. M. I. Diez-Garcia, R. Gomez, Investigating water splitting with $CaFe_2O_4$ photocathodes by electrochemical impedance spectroscopy. ACS Appl. Mater. Interfaces 8 (2016) 21387-97.
47. J. D. Benck, Z. Chen, L. Y. Kuritzky, A. J. Forman, T. F. Jaramillo, Amorphous molybdenum sulfide catalysts for electrochemical hydrogen production: insights into the origin of their catalytic activity. ACS Catal. 2 (2012) 1916-1923.
48. J. Kibsgaard, T. F. Jaramillo, Molybdenum phosphosulfide: an active, acid-stable, earth-abundant catalyst for the hydrogen evolution reaction. Angew. Chem. Int. Ed. 53 (2014) 14433-14437.
49. Y. Liu, X. Shang, W. Gao, B. Dong, J. Chi, X. Li, K. Yan, Y. Chai, Y. Liu, C. Liu, Ternary CoS_2/MoS_2/RGO electrocatalyst with CoMoS phase for efficient hydrogen evolution. Appl. Surf. Sci. 412 (2017) 138-145.
50. P. Sabhapathy, C. Liao, W. Chen, T. Chou, I. Shown, A. Sabbah, Y. Lin, J. Lee, M. Tsai, K. Chen, L. Chen, Highly efficient nitrogen and carbon coordinated N-Co-C

electrocatalysts on reduced grapheme oxide derived from vitamin-B12 for the hydrogen evolution reaction. J. Mater. Chem. A 7 (2019) 7179-7185.

51. N.-T. Suen, S.-F. Hung, Q. Quan, N. Zhang, Y.-J. Xu, H.-M. Chen, Electrocatalysis for the Oxygen Evolution Reaction: Recent Development and Future Perspectives. Chem. Soc. Rev. 46 (2017) 337-365.
52. M. Retuerto, F. Calle-Vallejo, L. Pascual, G. Lumbeeck, M.T. Fernandez-Diaz, M. Croft, J. Gopalakrishnan, M.A. Pena, J. Hadermann, M. Greenblatt, S. Rojas, $La_{1.5}Sr_{0.5}NiMn_{0.5}Ru_{0.5}O_6$ double perovskite with enhanced ORR/OER bifunctional catalytic activity. ACS Appl. Mater. Interfaces 11 (2019) 21454-21464.
53. S. Gao, H. Fan, X. Wei, L. Li, Y. Bando, D. Golberg, Nitrogen-doped carbon with mesopore confinement efficiently enhances the tolerance, sensitivity, and stability of a Pt catalyst for the oxygen reduction reaction. Part. Part. Syst. Charact. 30 (2013) 864-872.
54. A. Ashok, A. Kumar, M. A. Matin, F. Tarlochan, Probing the effect of combustion controlled surface alloying in silver and copper towards ORR and OER in alkaline medium. J. Electroanal. Chem. 844 (2019) 66-77.
55. B. Liu, L. Huo, R. Si, J. Liu, J. Zhang, A general method for constructing two-dimensional layered mesoporous mono- and binary-transition-metal nitride/graphene as an ultra-efficient support to enhance its catalytic activity and durability for electrocatalytic application. ACS Appl. Mater. Interfaces 8 (2016) 18770-18787.
56. K. Jukk, N. Kongi, K. Tammeveski, J. Solla-Gullón, J. M. Feliu, Electroreduction of oxygen on PdPt alloy nanocubes in alkaline and acidic media. ChemElectroChem 4 (2017) 2547-2555.
57. W. Jiao, C. Chen, W. You, G. Chen, S. Xue, J. Zhang, J. Liu, Y. Feng, P. Wang, Y. Wang, H. Wen, R. Che, Tuning strain effect and surface composition in PdAu hollow

nanospheres as highly efficient ORR electrocatalysts and SERS substrates. Appl. Catal. B 262 (2020) 118298.

58. L. Liu, Q. Wei, X. Yu, Y. Zhang, Metal-organic framework-derived Co_3O_4/Au heterostructure as a catalyst for efficient oxygen reduction. ACS Appl. Mater. Interfaces 10 (2018) 34068-34076.
59. B. Men, Y. Sun, Y. Tang, L. Zhang, Y. Chen, P. Wan, J. Pan, Highly dispersed Ag-functionalized graphene electrocatalyst for oxygen reduction reaction in energy-saving electrolysis of sodium carbonate. Ind. Eng. Chem. Res. 54 (2015) 7415-7422.